

www.acsami.org Research Article

Nanoscale Structure—Property Relations in Self-Regulated Polymer-Grafted Nanoparticle Composite Structures

Shawn M. Maguire, [∇] J. Brandon McClimon, [∇] Aria C. Zhang, Austin W. Keller, Connor R. Bilchak, Kohji Ohno, Robert W. Carpick,* and Russell J. Composto*



Cite This: ACS Appl. Mater. Interfaces 2023, 15, 10974–10985



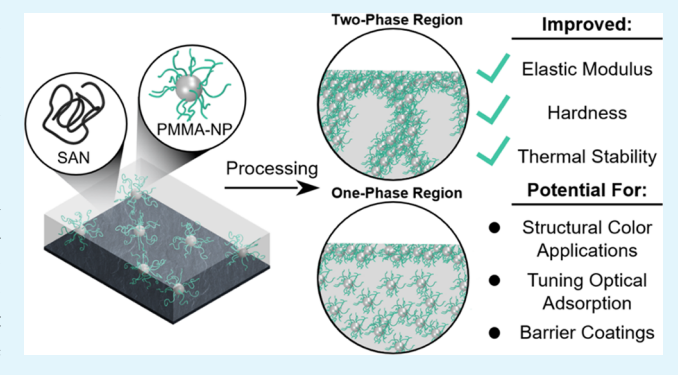
ACCESS I

III Metrics & More

Article Recommendations

sı Supporting Information

ABSTRACT: Using a model system of poly(methyl methacry-late)-grafted silica nanoparticles (PMMA-NP) and poly(styrene-ran-acrylonitrile) (SAN), we generate unique polymer nanocomposite (PNC) morphologies by balancing the degree of surface enrichment, phase separation, and wetting within the films. Depending on the annealing temperature and time, thin films undergo different stages of phase evolution, resulting in homogeneously dispersed systems at low temperatures, enriched PMMA-NP layers at the PNC interfaces at intermediate temperatures, and three-dimensional bicontinuous structures of PMMA-NP pillars sandwiched between two PMMA-NP wetting layers at high temperatures. Using a combination of atomic force microscopy (AFM), AFM nanoindentation, contact angle



goniometry, and optical microscopy, we show that these self-regulated structures lead to nanocomposites with increased elastic modulus, hardness, and thermal stability compared to analogous PMMA/SAN blends. These studies demonstrate the ability to reliably control the size and spatial correlations of both the surface-enriched and phase-separated nanocomposite microstructures, which have attractive technological applications where properties such as wettability, toughness, and wear resistance are important. In addition, these morphologies lend themselves to substantially broader applications, including: (1) structural color applications, (2) tuning optical adsorption, and (3) barrier coatings.

KEYWORDS: polymer interfaces, polymer nanocomposites, grafted nanoparticles, nanomechanics, thermal stability, self-regulated structures

■ INTRODUCTION

Polymer nanocomposites (PNCs) are a class of material consisting of a continuous organic polymer phase and a discrete inorganic phase often composed of nano-sized particles. PNCs combine the processability and cost-effectiveness of polymers with the emergent properties enabled by nanoparticles (NPs) to develop composite materials with properties often exceeding that expected from simple volumetric arguments. Additionally, the geometry and chemistry of the inorganic filler may influence the resultant properties since they affect both the surface energetics and surface-to-volume ratio. As such, PNCs offer the possibility of creating next-generation materials with substantially improved properties across a wide range of applications, including elastic modulus, damping, fracture toughness, hardness, ²⁻¹⁰ wear resistance, ¹¹⁻¹³ optical properties, ¹⁴⁻¹⁷ gas and solvent transport, ¹⁸⁻²¹ ion conductivity, ²²⁻²⁵ among many others. Akcora et al.² demonstrated that while the addition of silica NPs to a glassy polymer matrix always results in mechanical reinforcement, the effect is greatest when the NPs form largescale aggregates that percolate throughout the polymer phase

in a manner similar to the percolated minerals found in bone. ^{26,27} Therefore, the properties of PNC materials are often dictated by the dispersion state of the inorganic NP filler. In many instances, the properties of the PNC are optimized when the filler is well dispersed, although instances exist where limited aggregation or preferential localization of the NPs may be beneficial. ^{1,9} For example, gas diffusion in PNCs consisting of NPs with polymer chains end-grafted to their surface increases by an order of magnitude when the NPs remain well dispersed and are promising materials for separation membranes. However, PNCs with aggregated NPs exhibit substantially reduced gas transport and are ideal for barrier materials. Therefore, understanding and controlling the morphologies of PNCs are crucial challenges to address in

Received: September 1, 2022 Accepted: February 6, 2023 Published: February 17, 2023





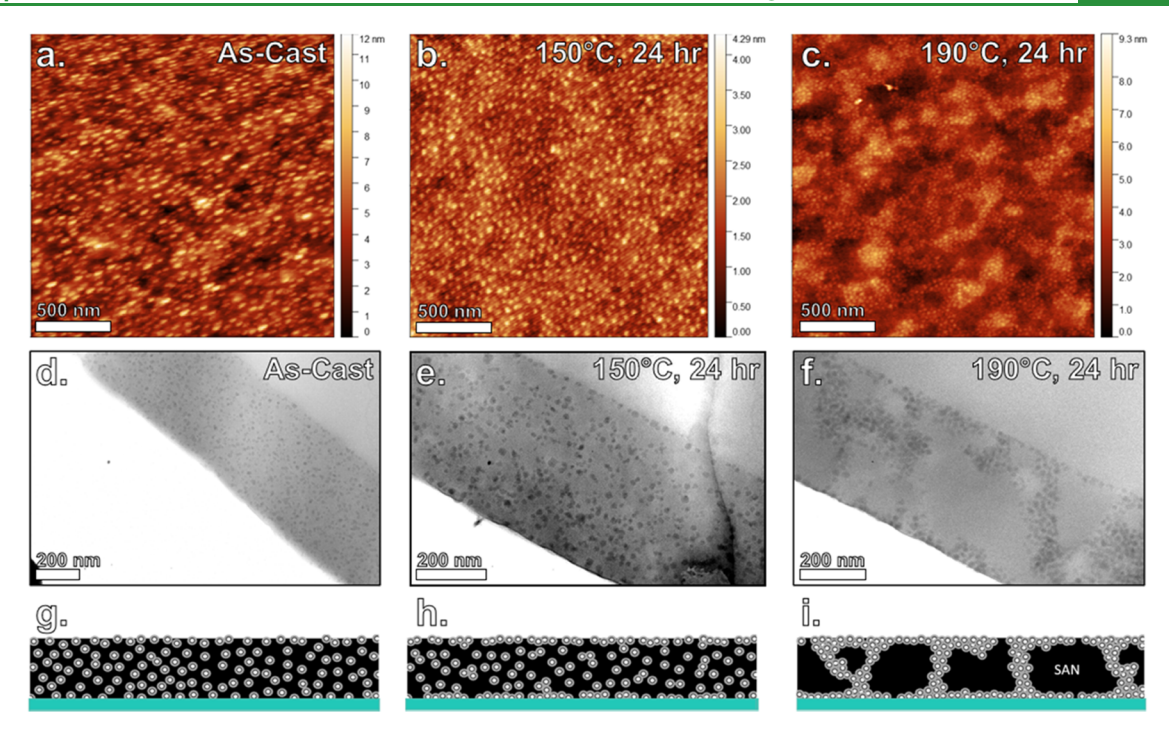


Figure 1. Surface morphology evolution of 25/75 wt % PMMA-NP/SAN films as evidenced through AFM height images (a) as-cast and films annealed in the (b) one-phase and (c) two-phase regions of the phase diagram for 24 h. Representative TEM cross-sectional images of the same 25/75 wt % PMMA-NP/SAN composite films display internal morphology evolution for (d) as-cast and annealed in the (e) one-phase and (f) two-phase regions. Below each TEM image is a cartoon representation of the cross-sectional view of the thin-film morphologies in each region (g-i).

the rational design of functional polymeric materials with desired property enhancements.

There are a wide variety of examples of self-assembled PNC materials in nature that have been built and optimized over billions of years. These have since become a source of inspiration for scientists and engineers and led to the field of biomimetics (i.e., the emulation of the models, systems, and elements of nature).²⁸ For example, based on the anatomy of sea cucumbers, 29,30 researchers recently created stimuliresponsive PNCs composed of cellulose nanocrystals (CNCs) that are grafted with a lower critical solution temperature (LCST) polymer embedded within a poly(vinyl acetate) (PVAc) matrix that increase their stiffness when exposed to warm water. Additionally, antibacterial PNC coatings have been developed based on a marine musselinspired method involving polydopamine as a biomimetic surface modifier. 31-33 Perhaps the most famous example is the natural composite nacre, which consists of a hierarchical structure of inorganic aragonite "bricks" and organic chitin "mortar". Nacre is found in seashells and has been extensively recognized for its remarkably high toughness and resilience. 28,34-36 Zhao et al. have recently replicated the brickand-mortar structure of nacre using self-assembled silica NPs using semicrystalline polymer growth fronts, where the crystallized morphology led to a dramatic improvement in the storage modulus.³⁷ Taken together, it is no surprise that scientists have been driven to investigate and model natures' architectures and compositions with the aim of developing analogous synthetic materials whose properties and performance exceed the current state of the art. However, achieving such complex structures through current technologies has been hindered by an inability to sufficiently control the self-assembly of NP fillers within PNC materials.

Herein, we utilize fundamental insights of Maguire et al. 38,39 about how the incorporation of poly(methyl methacrylate)grafted nanoparticles (PMMA-NP) modifies the thermodynamics phase space and evolution kinetics of the poly(methyl methacrylate)-poly(styrene-ran-acrylonitrile) (PMMA-SAN) material system to fabricate PNC morphologies that have the potential for bio-inspired applications with the aim of making these functional materials a reality. Specifically, the PMMA-NP/SAN system has a lower critical solution temperature (LCST) of 160 °C, readily allowing access to both the onephase and two-phase region of the PNC phase diagram. Here, we generate three distinct and novel polymer nanocomposite (PNC) morphologies by balancing the degree of surface enrichment, phase separation, and wetting within the films. Depending on the processing conditions (i.e., thermal treatment temperature and time), the thin films undergo different stages of phase evolution, resulting in: (1) homogeneously dispersed systems at low temperatures; (2) enriched PMMA-NP layers at both PNC interfaces while remaining uniformly dispersed in the bulk at intermediate temperatures; and (3) three-dimensional bicontinuous structures of PMMA-NP pillars sandwiched between two PMMA-NP wetting layers at high temperatures. Using a combination of atomic force microscopy (AFM), AFM nanoindentation, contact angle goniometry, and optical microscopy, we show that these self-regulated structures lead to nanocomposites with increased elastic modulus, hardness, and thermal stability compared to analogous PMMA/SAN blends. We highlight additional structure-property relationships that can utilize the phenomena presented in this study with support from recent literature, including structural color applications inspired by the iridescent colors of peacock feathers.

RESULTS AND DISCUSSION

By balancing the degree of surface enrichment, phase separation, and wetting within polymer-grafted nanoparticle composites, a variety of unique PNC morphologies were generated. Figure 1a-c shows representative AFM images of the PMMA-NP/SAN PNC surface with the height scale to the right of each image. The as-cast PNC (Figure 1a) shows uniformly dispersed PMMA-NPs, commensurate with what has been previously observed under similar loadings (note: slight distortions in Figure 1a are attributed to thermal drift). 38,40 Upon annealing in the one-phase region (Figure 1b) at 150 °C for 24 h, a qualitative increase in the number density of NPs at the free surface is observed. The NP number density appears to further increase upon annealing in the two-phase region (Figure 1c) at 190 °C for 24 h. To quantify this, image analysis has been performed to assess the particle number density on the surface as a function of annealing temperature following procedures previously published by Maguire et al. (see the Supporting Information for details). 38,40 For the ascast PMMA-NP/SAN film, the NP number density was found to be ca. 303 NP/ μ m². Upon annealing for 24 h at 150 °C and 190 °C, the NP number density increased to ca. 443 NP/ μ m² and ca. 605 NP/ μ m², respectfully. Under identical annealing conditions, Maguire et al. reported values of 302 \pm 24, 396 \pm 9, and 620 \pm 25 NP/ μ m² for as-cast, 150 °C-annealed, and 190 °C-annealed PNC films, respectfully, which is consistent with the values reported herein. 38,40 In addition to an increasing NP number density with increasing annealing temperature, the surface roughness decreases upon annealing when compared to as-cast films. This is evidenced by the calculated root-mean-square roughness (R_d) values obtained from the AFM images presented in Figure 1a-c: $R_q \sim 1.5$ nm (as-cast), $R_q \sim 0.6$ nm (150 °C), and $R_q \sim 0.9$ nm (190 °C).

Figure 1d-f shows a series of representative cross-sectional TEM images of the same 25/75 wt % PMMA-NP/SAN films displaying internal morphology evolution after annealing in both the (e) one-phase and (f) two-phase regions of the PNC phase diagram. An as-cast image (Figure 1d) is included here to show that the initial starting morphologies of the PNC reveal predominantly isolated and uniformly dispersed PMMA-NPs (i.e., homogeneous initial state). The PNC morphologies were induced by spin-coating ca. 450 nm thin films, followed by thermal annealing at 150 °C (one-phase) and 190 °C (twophase) for 24 h under continuous argon flow following procedures previously described by Maguire et al. 38,40 These temperatures are higher than the glass-transition temperature of the constituents (i.e., $\Delta T_{\rm g,150~^{\circ}C} \approx 30~^{\circ}$ C, $\Delta T_{\rm g,190~^{\circ}C} \approx 70~^{\circ}$ C). As seen in Figure 1e, the sample annealed in the one-phase region exhibits dispersed PMMA-NPs throughout the thickness of the film, with an enriched concentration of NPs at the free surface relative to the bulk. We note that in Figure 1e there appears to be the formation of small NP clusters when annealed at temperatures $T_{LCST} > T > T_g$ even though macrophase separation is not thermodynamically favorable. Annealing the samples above their glass transition allows the NPs to diffuse more readily, leading to the formation of small clusters due to the short-range attractive forces between the particles as noted in previous work.³⁹ Figure 1f shows the formation of a trilayer structure, PMMA-NP rich/SAN rich/ PMMA-NP rich, that forms parallel to the substrate. Specifically, columnar-like structures of PMMA-NP aggregates span two PMMA-NP wetting layers and are surrounded by a

SAN-rich phase. While PMMA-NP cores appear smaller in Figure 1d compared to Figure 1e,f, ImageJ analysis (Figure S1) reveals that the NP cores are the same diameter between each annealing condition upon taking the change in scale bar into consideration (i.e., 14.1 ± 4.6 , 13.9 ± 4.1 , and 14.9 ± 4.1 nm for as-cast, 150 °C-annealed, and 190 °C-annealed PNC films, respectfully). For clarity, schematic representations of the different cross-sectional morphologies are shown below each TEM image in Figure 1g–i.

The polymer physics underpinning the development of these PNC morphologies are the following: (1) at room temperature, the PNC films are kinetically trapped upon processing. (2) When annealed in the one-phase region of the phase diagram at temperatures $T > T_{\rm g}$, surface segregation of the lower-surface-energy component (PMMA-NP) competes with the bulk thermodynamic contributions (i.e., the Flory-Huggins interaction parameter, χ) that favors uniform mixing of SAN and PMMA-NPs. This results in the formation of a near-monolayer of PMMA-NPs at the free surface, with a uniform dispersion in the bulk. (3) Upon annealing in the twophase region of the phase diagram, surface segregation of the lower-surface-energy component and χ mutually enhance surface wetting of the PMMA-NPs. Simultaneously, columnar-like structures of PMMA-NPs form due to the hydrodynamic flow-driven wetting that occurs during phase separation.⁴¹ Here, we utilize these polymer physics concepts and investigate the property enhancements that result from such PNC formations.

Mechanical Properties. The mechanical properties (i.e., elastic modulus and hardness) of the different PMMA-NP/ SAN morphological systems were first evaluated by depthsensing indentation (DSI) on spun-cast thin films with a thickness of ca. 450 nm. Here, due to the film thickness and small depth of indentation needed, atomic force microscopy (AFM) was utilized as a depth-sensing instrument (i.e., AFM nanoindentation). Traditionally, the reduced modulus and hardness of the sample are inferred from the analysis of the load-displacement curves subsequent to indentation with a tip of known geometry. In this work, AFM nanoindentation for all PNC samples was performed at a rate of 100 nm/s and up to a maximum load of 300-1200 nN, which corresponds to an indentation depth less than 10% of the film thickness to avoid substrate effects. The Oliver-Pharr analysis methodology is utilized with an accurate area function calculated from TEM imaging of the AFM tip apex. 42 The indentation hardness values we report to characterize the yield behavior of the nanocomposite are specific to the indentation geometry and protocol.⁴³ Also, it should be noted that slow plastic recovery is common in polymer systems which creates ambiguity in the definition of polymer hardness.⁴⁴ The surface morphology of the PNC films was observed using atomic force microscopy in tapping mode before and after nanoindentation.

To investigate if the jammed NP columnar-like structures resist deformation more so than the enriched NP layer at the free surface, AFM nanoindentation experiments were performed on 25/75 wt % PMMA-NP/SAN films annealed in both the one-phase and two-phase region of the phase diagram. As shown in Figure 1e, the samples annealed at 150 °C exhibit an enrichment of PMMA-NPs at the free surface of the film relative to the bulk, but without the formation of PMMA-NP columnar-like structures evident in Figure 1f. Therefore, a direct comparison between the mechanical properties of these two annealed samples should

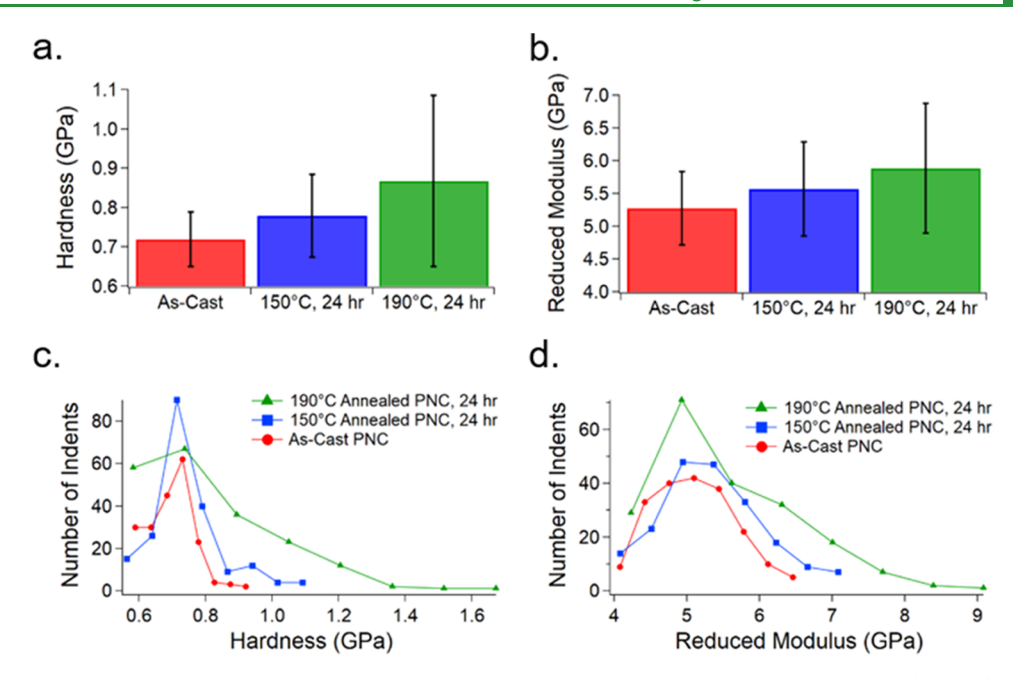


Figure 2. Mechanical properties of 25/75 wt % PMMA-NP/SAN PNC films as-cast, and annealed in the one-phase (150 °C) and two-phase (190 °C) regions of the phase diagram for 24 h. (a) Plots the PNCs hardness as a function of the annealing temperature. Error bars are standard deviations of the properties measured across 200 indents in each sample. (b) Plots the PNCs reduced modulus under identical annealing temperatures. (c, d) Plots the same PNC hardness and reduced modulus values from (a, b), but against the number of AFM nanoindentations. Here, the distribution of values grows upon increasing the annealing temperature and time, with the growth of a high modulus and hardness tail. This tail is responsible for the increasingly larger error bars in (a, b) with annealing temperature.

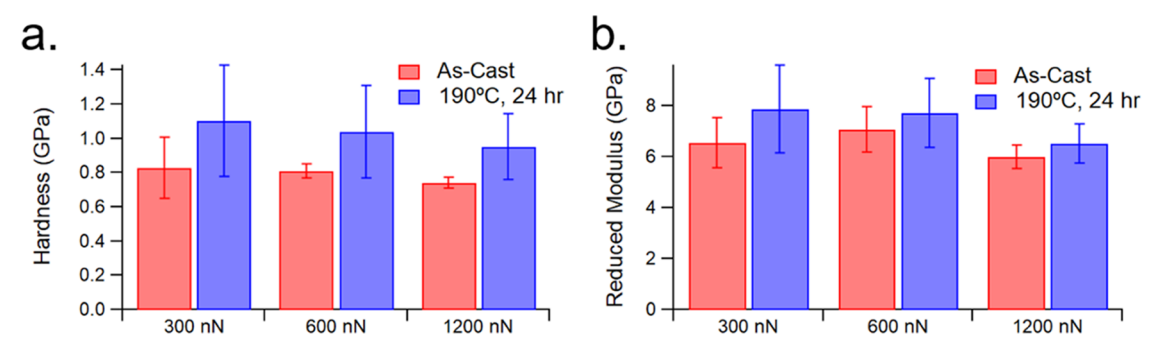


Figure 3. Mechanical properties of the 25/75 wt % PMMA-NP/SAN films before and after annealing at 190 °C for 24 h as measured through AFM nanoindentation. (a) Plots the PNCs hardness as a function of the peak indentation load (i.e., deeper indents). (b) Plots the PNCs reduced modulus under identical peak loadings. Error bars represent the standard deviation of properties measured across each pattern of indents.

help elucidate which NP morphology is contributing to the property enhancements the most. Figure 2a,b plots the hardness and reduced modulus, respectively, for 24 h 150 °C- and 190 °C-annealed films with an as-cast film plotted for reference. The error bars show the standard deviation of the properties measured across 200 individual indents in each sample. A monotonic increase in both hardness and reduced modulus are achieved with increasing annealing temperature. Interestingly, the change in hardness and reduced modulus between the as-cast and 150 °C-annealed films is comparable to the change between the 150 and 190 °C films. Figure 2c,d plots the same PNC hardness and reduced modulus values from Figure 2a,b, but against the number of AFM nanoindentations. Here, the distribution of values grows upon increasing the annealing temperature and time, with the growth of a high modulus and hardness tail. This tail is responsible for the increasingly larger error bars in Figure 2a,b with annealing temperature. Taken together, these results suggest that the enrichment of PMMA-NPs enhances the

hardness and reduced modulus of the films, but the improvements are further increased upon the morphological development of the PMMA-NP columnar-like structures that span the two enriched layers. Due to the LCST nature of this PMMA-NP/SAN composite, it is not unreasonable to presume that the mechanical properties of the one-phase and two-phase PNCs are reversibly accessible given sufficient annealing times. Reversible accessibility in LCST systems has been discussed and demonstrated by Bockstaller et al. during their investigation of PMMA-NP/SAN-NP composite phase behavior, systems very similar to those presented in the current study. 45

Figure 3a,b plots the hardness and reduced modulus, respectively, for an as-cast and 24 h 190 °C-annealed 25/75 wt % PMMA-NP/SAN film as a function of peak indentation load. Note: data were obtained from areas distinct from those shown in Figure 2. Here, each peak indentation load corresponds to an approximate indentation depth of: 300 nN = 3-6 nm, 600 nN = 12-15 nm, and 1200 nN = 34-43 nm.

To illustrate the relevant length scales, a schematic representation of the AFM nanoindentation experiments, with the tip and nanoparticles shown approximately to scale, performed on the three 25/75 wt % PMMA-NP/SAN PNC films is displayed in Figure 4a–c, with the indentation depths

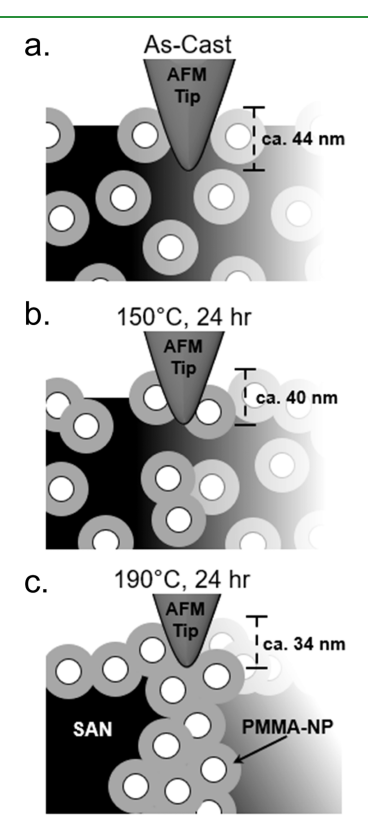


Figure 4. Schematic representations of the AFM tip indenting the (a) as-cast, (b) 150 $^{\circ}$ C-, and (c) 190 $^{\circ}$ C-annealed PNC surfaces. Note: indent depths correspond to an indentation load of 1200 nN.

chosen to correspond to the approximate average value attained at a peak load of 1200 nN. From Figures 2 and 3, it is revealed that the unique nanocomposite structures generated through thermal annealing (Figure 1) lend themselves to mechanical reinforcement, with an increase in both hardness and modulus compared to as-cast films. We note that the relative increase in both hardness and reduced modulus upon thermal annealing decreases with increasing peak indentation load (i.e., deeper indents). This can be attributed to increasing indentation size effects wherein indentation measured hardness and modulus decrease with increasing maximum indentation depth. 46 This effect is ubiquitously observed in polymeric samples. While previous experiments helped shed light onto the different morphological effects on the resultant mechanical behavior, one important question still remains: are the local mechanical enhancements predominantly due to (1) the increased local particle density at the free surface, or (2) reinforcement from the jammed particle columnar-like structures that span the thickness of the film?

Figure 5 depicts AFM images of the 25/75 wt % PMMA-NP/SAN PNC post indentation for an (a) as-cast sample and (b) one that has been annealed at 190 °C for 24 h. The indentations on the as-cast PNC are homogeneous and reach a consistent depth, while the indentations for the annealed sample are inhomogeneous in both depth and lateral area. An example highlighting the difference between a deep and

shallow indent under an identical peak load is shown in Figure 5b, denoted by a teal and purple circle, respectively. These images demonstrate that in addition to the ability to measure properties, AFM imaging before and after indentation allows for the correlation of local properties with local topography, specifically the locations of near-surface nanoparticles. By increasing the indent density so that nearby nanoparticle-rich and -poor areas can be indented within a single pattern, local property maps can be generated and overlaid on pre-indent images of the same regions. Figure 5c,d displays hardness property maps of the same as-cast and annealed PNC films as in Figure 5a,b but with indents more closely spaced, 56 nm vs 222 nm spacing, than in Figure 5a,b. Commensurate with the post-indentation AFM images, the hardness map of the annealed PNC film displays lateral inhomogeneity relative to the as-cast sample (see Figure S5 for corresponding reduced modulus maps). The regions of increased hardness are responsible for the shallower residual indendation depths, as evident in the example shown in Figure 5b. Due to the lateral inhomogeneity in indentation depths as well as commensurate length scales between the indents with increased hardness and the NP pillars evident in Figure 1f, we attempt to address our previously proposed question and hypothesize that the mechanical enhancements are predominantly due to the pillar formation.

To further probe the effect of the columnar-like structures, we examined the mechanical properties of the subsurface via AFM nanomilling. In AFM nanomilling, contact mode imaging is utilized to wear away the surface layer of the film, to a depth of 40-80 nm. This depth is sufficient to remove the wetting layer of PMMA-NPs in the 190 °C-annealed film, as confirmed by tapping mode imaging of the milled region of the film. Properties derived from indent patterns in both milled and unmilled regions of the same PNC film were compared, as presented in Figure 6. While the subsurface of the annealed film does have lower average modulus and reduced hardness, likely due to being predominantly composed of SAN, the continuing presence of a high property tail that overlaps with the property distribution of the film surface indicates that the columnar-like structures greatly improve the mechanical properties locally. Here, it is important to note that this columnar-like morphology is only achieved under specific film thickness conditions and loadings of PMMA-NPs, one of which is denoted herein (i.e., ca. 450 nm thick, 25 wt % PMMA-NP). As shown in a PMMA/SAN morphology map derived by Chung and co-workers, variations in film thickness (i.e., 50-1000 nm) and PMMA volume fraction (i.e., 0.25-0.85) can lead to six distinct pattern development regimes, including discrete or fully percolated PMMA-rich domains.⁴¹ While the mechanical enhancements demonstrated herein are modest, it is likely possible to improve both the stiffening and hardening of the nanocomposite through facile changes in experimental parameters (e.g., brush length, grafting density, NP shape, NP size, NP loading, film thickness, etc.) leading to more jammed structures composed of PMMA-NPs. Additionally, utilizing the presented phenomenon in a PNC composed of grafted NPs in a softer matrix (i.e., nonglassy polymer) could be an exciting route to see far greater improvements in mechanical properties upon surface enrichment and columnar formation of the inorganic NPs.

Mechanical property enhancements of composites similar to those described above have been observed in nanocomposites produced using the capillary rise infiltration (CaRI) method. In

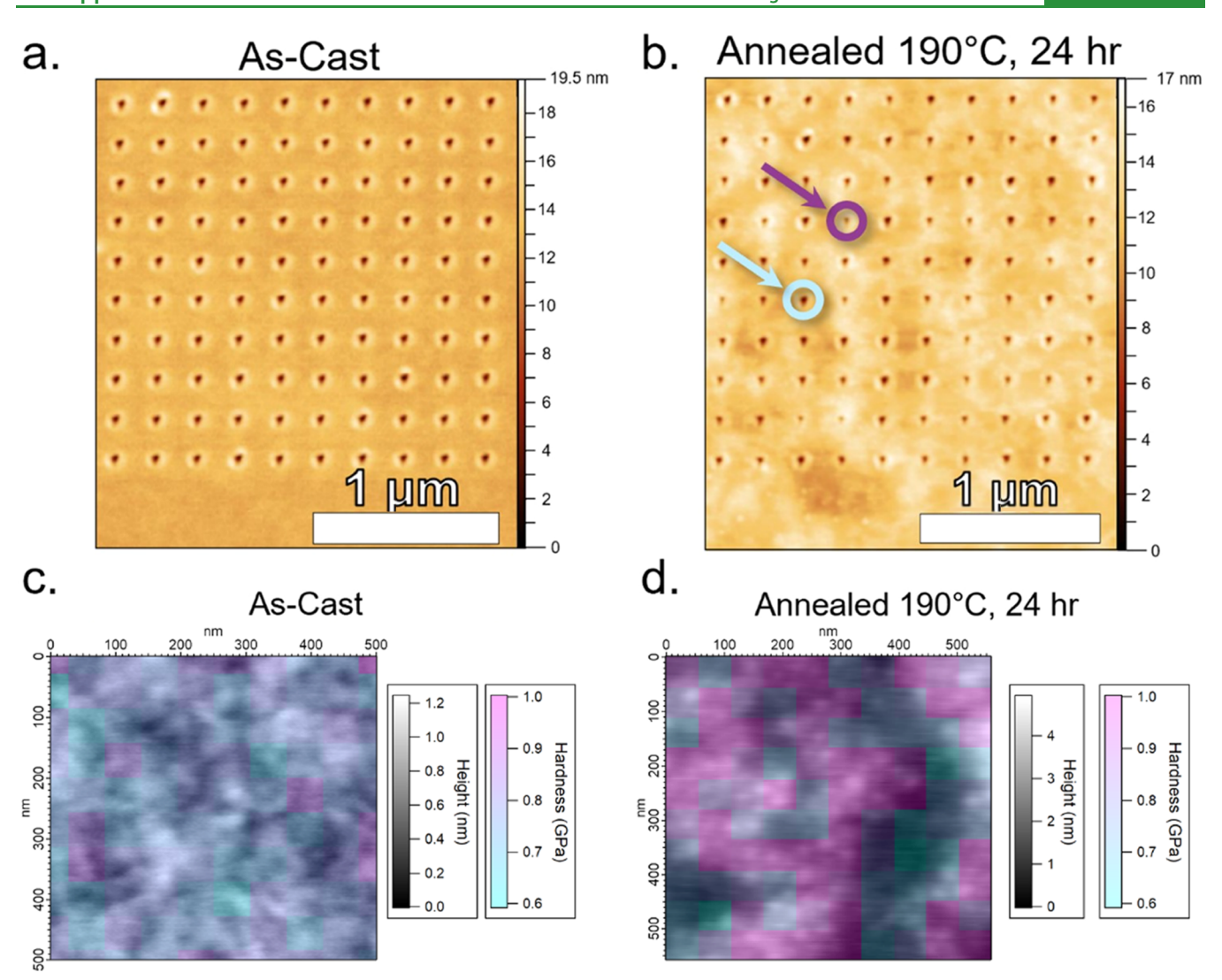


Figure 5. Atomic force microscopy (AFM) analysis of the surface of a 25/75 wt % PMMA-NP/SAN film as-cast and annealed at 190 °C for 24 h. (a, b) AFM images of the as-cast and annealed PNC surface after performing 100 nanoindentations, respectively. Additionally, teal and purple circles highlighted in (b) show a deep and shallow indent under identical peak load, respectively. (c, d) Hardness property maps of the same PNC films, obtained at different locations than (a, b). Note: the indents for the property maps are much closer together than in (a, b).

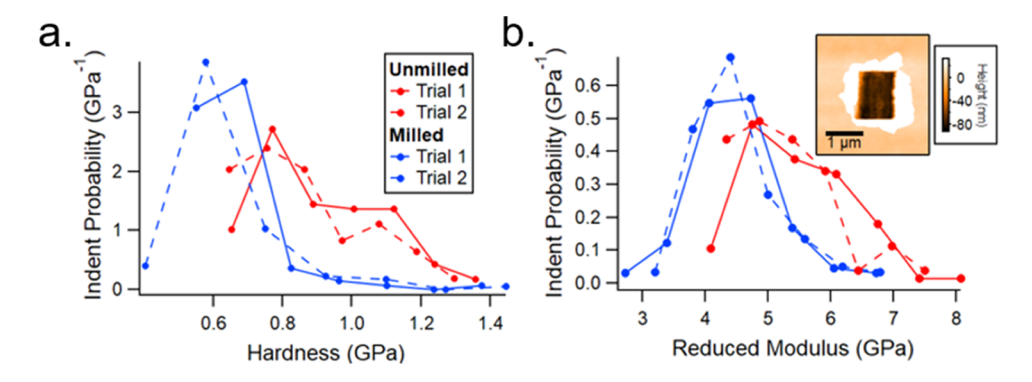


Figure 6. (a) Hardness and (b) reduced modulus of milled and unmilled regions of 25/75 wt % PNC films annealed in the two-phase (190 °C) region of the phase diagram for 24 h. The inset in (b) shows a tapping mode AFM image of a region that was milled with the AFM probe tip.

that work, densely packed NP layers are infiltrated with polymer melt via capillary forces, generating PNC films with extremely high nanofiller concentrations. Those films have shown promising property enhancements, specifically, increased hardness and elastic modulus.¹¹ In addition, the high

nanofiller fraction (>50 vol %) in CaRI leads to a significant enhancement in nanoscale wear and scratch resistance. ¹¹ Other high inorganic loading PNCs include recently developed polymer infiltrated scaffold metal (PrISM) composites that utilize a similar capillary infiltration method, resulting in

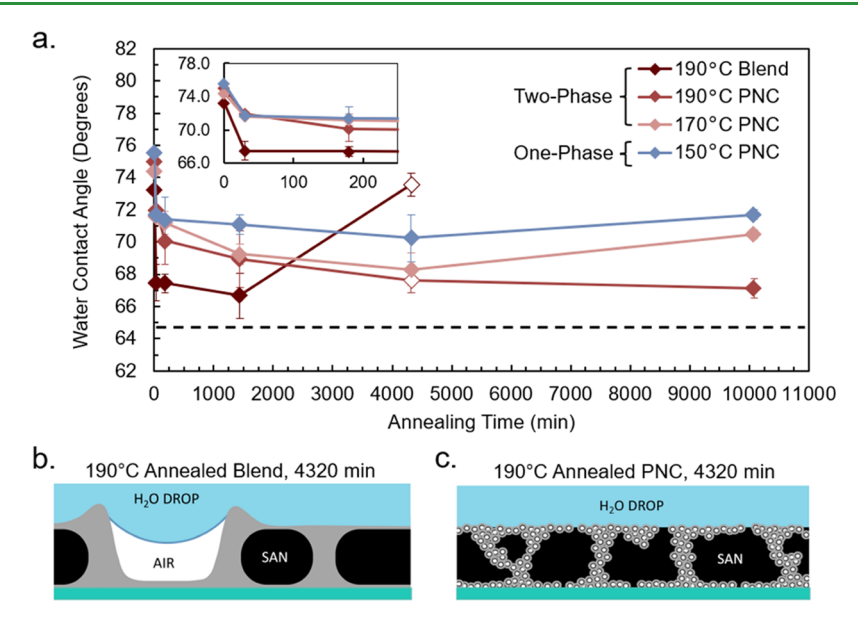


Figure 7. Water contact angle measurements of a 25/75 wt % PMMA/SAN and PMMA-NP/SAN film annealed at different temperatures for varying amounts of time. The dashed line is the water contact angle of a pure PMMA homopolymer film. The inset in (a) plots the same data on a shorter *x*-axis, highlighting the wetting behavior at short times. (b, c) Cross-sectional schematics of the PMMA/SAN and PMMA-NP/SAN films, respectively, after 4320 min of thermal annealing at 190 °C (note: the open data symbols in (a) correspond to these two conditions).

bicontinuous polymer/metal hybrids. ⁴⁷ Akin to the CaRI films, these PrISM composites are anticipated to display increased hardness, modulus, as well as viscoelastic properties relative to the individual constituents due to the bicontinuous hard (metal) and soft (polymer) phases. Importantly, the method presented herein generates PNC films with increased mechanical properties while utilizing significantly less inorganic filler (\ll 50 vol %) in comparison to the CaRI and PrISM composites.

Thermal Stability. We now move to discussing the thermal stability of these unique PNC morphologies below their degradation temperatures, where thermal stability refers to the PNC film stability. Polymer blends are susceptible to thermally induced dewetting. The thermal stability of the PNC should be improved relative to the polymer blend because the jammed NP layers and NP columnar structures should resist deformation, similar to what we observed using AFM nanoindentation. Previously, it was demonstrated that polystyrene nanoparticles will strongly segregate to the substrate interface and form a monolayer upon annealing within a polystyrene matrix, leading to dewetting inhibition. 48,49 Similarly, cadmium selenide QDs also inhibit dewetting of polystyrene thin films when a monolayer of QDs is formed at the air interface. 48 Taken together, these results suggest that the presence of a layer of NPs at either the free surface or substrate interface prevents the dewetting of polymer films. For the case of symmetric wetting layers of NPs, preliminary results obtained by Maguire et al. suggest comparable behavior,³⁸ where the PNC morphology shown in Figure 1c appears to be thermally stable for annealing times up to 3 days at 190 °C as evident by the films' low root-meansquare roughness values. Unlike the analogous 25/75 wt % PMMA/SAN polymer blend where the film dewets during the late-stage evolution of phase separation, the jamming of the PMMA-NPs at both interfaces arrests the morphology. Specifically, the NPs halt interfacial roughening, which is the main contribution to film rupture, and therefore increases film

thermal stability. A thorough discussion of this phenomenon is presented in the Supporting Information (see Figure S7).

To experimentally probe the improved thermal stability of these PNC films due to the jamming of PMMA-NPs, water contact angle measurements were obtained as a function of thermal annealing temperature and time. Figure 7 shows representative contact angle measurements of a 25/75 wt % PMMA-NP/SAN film annealed in the one-phase (blue curve) and two-phase (red curves) region of the phase diagram relative to the PMMA/SAN blend analogue as a function of annealing time. In addition, the water contact angle of a pure PMMA homopolymer film (19 kg/mol) is plotted and has a water contact angle of ca. 65° (note: this is slightly lower than the average reported value of ca. 68°, but within the range of other published quantities^{50,51}). While not plotted, the water contact angle of a pure SAN film was found to be $78.2^{\circ} \pm 1$. For the 25/75 wt % PMMA-NP/SAN film annealed at all temperatures, the contact angle decreases with time. The samples annealed at the highest temperature (i.e., 190 °C) have a water contact angle approaching that of pure PMMA. This decrease in contact angle is commensurate with what was observed using cross-sectional TEM (Figure 1), where the surface becomes more hydrophilic during phase separation with PMMA-NPs enriching the free surface. Additionally, the extent of PMMA-NP surface enrichment is dependent on the annealing temperature, as noted previously.³⁸ This extent has been previously quantified for samples prepared under identical conditions using grazing-incidence Rutherford backscattering spectrometry (GI-RBS) by Maguire et al. (see Figure S9).

Interestingly, the contact angle for the PMMA/SAN blend decreases rapidly and approaches that of pure PMMA for short annealing times (see Figure 7a, inset). However, as the sample is annealed for times that approach the late stage of spinodal decomposition, the contact angle increases rapidly (ca. 72 h). This suggests that the polymer blend film is beginning to dewet, and film rupture is occurring. As the films begin to dewet and form pin-holes smaller than the capillary length of

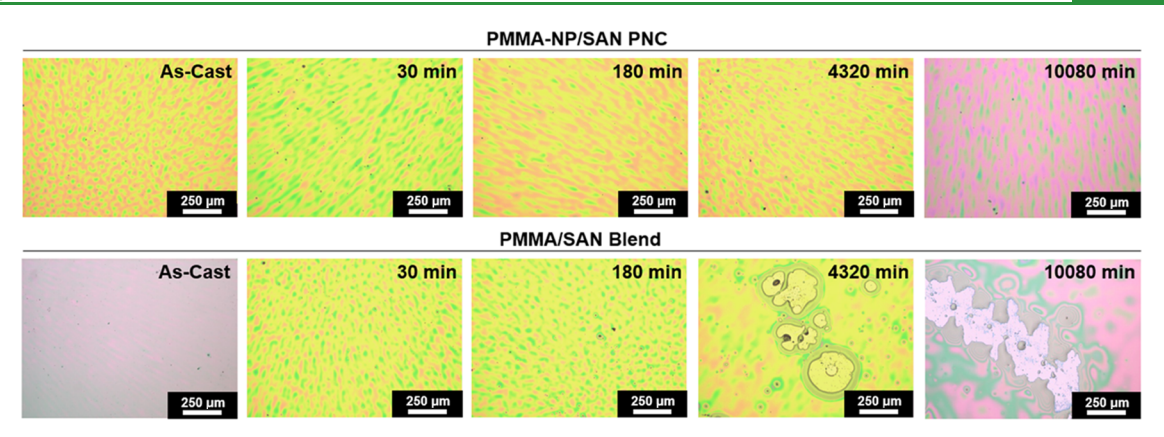


Figure 8. Optical microscopy images of (top) 25/75 wt % PMMA-NP/SAN and (bottom) 25/75 wt % PMMA/SAN films annealed at 190 °C for up to 168 h, respectively, using a 10× objective lens and 1.67× relay lens.

water (ca. 2 mm), the water contact angle is determined by the balance between the PMMA enriched layer and air gaps. Since air creates a contact angle of 180°, the increase in water contact angle at 72 h (4320 min) is expected and can be quantified using the Cassie-Baxter equation. A schematic representation of the 190 °C 72 h annealed PMMA/SAN film and the 190 °C 72 h annealed PMMA-NP/SAN film behavior is shown in Figure 7b,c (note: these two conditions correspond to the open symbols in Figure 7a).

To complement the water contact angle measurements, optical microscopy images were taken of PMMA/SAN and PMMA-NP/SAN films annealed at 190 °C to monitor their dewetting behavior as a function of annealing time. It is evident that after 168 h of annealing, the nanocomposite film remains stable, with a homogeneous surface morphology (Figure 8, top). Conversely, the bottom row of Figure 8 demonstrates that the polymer blend is unstable after only 72 h, with clear dewetting of the film occurring. Both the water contact angle measurements as well as the optical microscopy images support the hypothesis that the interfacially jammed PMMA-NPs halt the formation of long-wavelength fluctuations at the surface, and suppress film rupture, even for annealing times ca. 2.5× longer than previously investigated by Maguire et al.³⁸ Here, we note the importance of the substrate utilized in these experiments (i.e., silicon with a native oxide layer). Due to a large difference in surface energies between PMMA-NP and SAN, as well as the preferential attraction of PMMA to the oxide substrate, PMMA-NPs dictate morphological development. 41 This leads to PMMA-NP-rich domains symmetrically wetting both the free surface and silicon substrate, leading to interfacial jamming of NPs. If the substrate chemistry was changed such that it was SAN-selective, it is not unreasonable to presume the resultant morphology would be different specifically with the lack of PMMA-NPs jammed at the two confining interfaces. As such, the films may behave akin to the blend analogue in which the film dewets from the substrate at elevated temperatures and long annealing times.

Potential Applications. So far, this work has highlighted two structure-property relationships that result from the unique PNC morphologies generated in this paper by balancing the degree of surface enrichment: phase separation, and wetting within the films. While the presented study focuses on a model system, we expect that the applications of such fundamental polymer physics concepts discussed herein, as well as their resultant PNC morphologies, may be substantially broader, including: (1) structural color applications, (2) tuning

optical adsorption, and (3) barrier coatings; these are highlighted in Figure S10. For support, we quickly highlight several key pieces of literature. Case 1: Fernández-Rico et al. recently highlighted that material scientists need the ability to arrest and control phase separation in synthetic materials with a high level of precision at multiple length scales, citing its critical importance for designing and synthesizing nextgeneration photonic materials. 52 Herein, we demonstrate the ability to control the degree of NP interfacial enrichment and bulk ordering in PNC films by tuning the annealing temperature and time, analogous to the arrangement of melanin rods during feather development in certain avian species.⁵³ Case 2: It is well known that various arrangements of metal NPs (e.g., gold, silver, etc.) lead to plasmonic structures, which are often constructed through the use of templates or organic grafts. 54,55 Here, the plasmonic properties of the metal NPs are highly sensitive to both their orientation and dispersion state (e.g., center-to-center interparticle distance, shape anisotropy, etc.). The readily accessible LCST of the PMMA-NP/SAN PNC system offers a unique opportunity to complement traditional methods of generating plasmonic materials that result in static distances between NPs (i.e., fixed plasmon coupling). For instance, substitution of the SiO₂ NP core with a metallic NP should result in a material system that has the potential to reversibly tune the plasmon resonance of NPs depending on the annealing temperature and time. Case 3: The PNC morphologies demonstrated in Figure 1 may be advantageous for barrier coatings due to the fact that SiO₂ NPs can organize at the film interfaces to increase scratch and wear resistance (i.e., mechanical properties) while remaining uniformly dispersed in the bulk of the film to maximize its tortuosity. Studies are currently underway investigating the applications discussed in cases 1-3 and will be presented in future work.

CONCLUSIONS

This manuscript has outlined different strategies to design selfregulated PNC morphologies with enhanced properties, including improved modulus, hardness, and thermal stability compared to analogous polymer blend systems. Specifically, this work utilizes the thermodynamic and dynamic insights obtained from previous studies to create PNCs with decoupled bulk and surface morphologies. By understanding the thermodynamics and kinetics of NP assembly in polymer matrices in this way, new PNC films with precise structureproperty relations can be developed. The morphologies

demonstrated herein lend themselves to additional applications as well, including those in (1) structural color applications, (2) tuning optical adsorption, and (3) barrier coatings.

EXPERIMENTAL SECTION

Sample Preparation. Poly(styrene-ran-acrylonitrile) (SAN) (M_w = 118 kg/mol, $M_{\rm w}/M_{\rm n}$ = 2.24, $T_{\rm g}$ = 114 °C, containing 33 wt % acrylonitrile) was provided by Monsanto and purified twice by adding a solution of SAN and chloroform (≥99.9%, for HPLC) into methanol (≥99.9%, for HPLC) at a 1:10 volume ratio following procedures described by Gam et al.⁵⁶ After allowing SAN to precipitate for 1 h, the solvent was removed, and the precipitant was dried for 48 h. Once dried, the SAN was redissolved in chloroform and precipitated with methanol once more. Here, SAN containing 33 wt % acrylonitrile was selected due to the unique phase behavior of this copolymer with PMMA. As the relative fraction of polystyrene to acrylonitrile changes, the Flory-Huggins interaction parameter between SAN/PMMA changes. Importantly, at the selected composition, this material system displays an accessible lower critical temperature (LCST) of ca. 160 °C that allows for experimental probing of both the one-phase and two-phase regions of the phase diagram. Silica nanoparticles (15 nm diameter) grafted with PMMA brushes, denoted as PMMA-NPs, were prepared using surface-initiated atom transfer radical polymerization. 57 The brush weight-average molecular weight and grafting density were 19 kg/mol and 0.7 chains/nm², respectively, as determined by thermogravimetric analysis (TGA, TA Instruments Q600 SDT) at a heating rate of 10 °C/min under argon flow between the temperatures of 25 and 550 °C. The glass-transition temperature (T_g) of each polymer was measured using a differential scanning calorimeter (TA Instruments Q2000) between the temperatures of 25 and 150 °C. In all cases, two heating/cooling cycles were performed at a heating/cooling rate of 5 $^{\circ}$ C/min. The T_{α} values were obtained from the second heating to eliminate any thermal history. The hydrodynamic radius of the PMMA-NPs was determined to be 19 nm by dynamic light scattering (DLS, Malvern Zetasizer nano-s). Details of TGA, differential scanning calorimetry, and DLS characterization of SAN and PMMA-NPs are given in the Supporting Information of our previous work.³⁹ At all experimentally probed temperatures, the surface energy of PMMA is less than that of the SAN matrix.³⁸ EpoxiCure 2 epoxy hardener and epoxy resin were purchased from Buehler. N-type, oriented silicon wafers (dopant Ph, 10–20 Ω·cm resistivity, 475–575 μ m thickness, single-side-polished) were purchased from Silicon Quest International. P-type, oriented silicon wafers (dopant B, 0.001-0.005 Ω ·cm resistivity, 500 μ m thickness, single-side-polished) with a 300 nm wet thermal oxide layer were purchased from University Wafer.

Films of the PNCs were prepared by spin-coating solutions (10 wt % solids in solvent) of the components in methyl isobutyl ketone (MIBK, ≥98.5%, Certified ACS, Fisher Chemical) onto different substrates; film thicknesses were ca. 450 nm. Samples were dried at 100 °C for 1 h to remove residual solvent. Following drying, the samples were annealed on a hot stage between 150 and 190 °C for varying amounts of time under continuous argon flow and then quickly quenched below the glass-transition temperature (ca. 120 °C) to "freeze" the morphologies.

Transmission Electron Microscopy. To prepare the samples for TEM characterization, the 10 wt % PNC solutions were spin-coated (4000 rpm, 60 s) onto 1 cm × 1 cm silicon wafers with a 300 nm thermal oxide layer and then dried at 100 °C for 1 h to remove the residual solvent. Following drying and annealing at 150 °C for various amounts of time, the PNC films were lifted from their substrates. To do this, the edges of the substrates were scored with a diamond knife and then floated on a 1:5 vol % solution of NaOH (50% w/w NaOH) and DI H2O. After lifting from its substrate, the films were transferred from the liquid-air interface of the NaOH solution to DI H2O and then onto Teflon. The specimens were then sandwiched between two pieces of tape, with an open window on one side to expose the free surface of the PNC. Next, the samples were embedded in two-part

epoxy (see Supporting Information). Once the epoxy cured, ~70 to 100 nm thick cross sections of the PNCs were prepared by ultramicrotomy (Leica Ultracut S Ultramicrotome) with a roomtemperature diamond knife. TEM characterization of the ultramicrotomed cross sections, transferred onto carbon-coated TEM grids, was performed with a JEOL JEM-1400 TEM operated at 120 kV. Average diameters and standard deviations were obtained for PMMA-NP cores shown in Figure 1d-f by analyzing ca. 400 unique NPs in each micrograph using ImageJ software.

Optical Microscopy. To compare the dewetting behavior of the PMMA/SAN blend and PMMA-NP/SAN PNC, solutions were prepared by dissolving the constituents in MIBK and stirred for 24 h using a magnetic stir bar. Both solutions (10 wt % in MIBK) were spin-coated (4000 rpm, 60 s) onto 1 cm x 1 cm silicon wafers with no thermal oxide layer, and then dried using the aforementioned procedure. After thermal annealing at 190 ${\rm ^{\circ}\bar{C}}$ for varying amounts of time, the samples were examined by optical microscopy (Olympus BH-2) in reflected light configuration using a 10× objective lens and 1.67× relay lens.

Contact Angle Goniometry. To investigate the thermal stability of the PMMA-NP/SAN PNC compared to the neat polymer analogue, water contact angle measurements were obtained as a function of thermal annealing temperature and time using a homebuilt water contact angle goniometer. Uniform water droplets were deposited onto the sample surface using a Gilmont Micrometer Dispenser and illuminated using a Stocker Yale Imagelite Lite Mite-Model 20. Equilibrium snapshots of the water droplets were captured using a Sony CCD N50 Video Camera Module with a Navitar Zoom 7000 close-focusing macro video lens mounted on an optical table. The snapshots were then analyzed using LB-ADSA—a Java plug-in for ImageJ software that is based on the fitting of the Young-Laplace equation to the water droplet. For each annealing temperature and time, three different snapshots were obtained at unique locations on the film surface, analyzed using this procedure, and averaged to obtain a standard deviation.

Standard AFM and AFM Nanoindentation. Standard AFM tapping mode measurements were performed using an Agilent 5420 AFM with noncontact tips (TAP300AL-G-50 radius of curvature <10 nm, Ted Pella) as a function of thermal annealing temperature and time. All AFM images were processed using Gwyddion software. Measurements were performed at ambient temperature and humidity (30-50% RH) after completion of the annealing treatment, if applicable. The PMMA-NP number density at the free surface was quantified by ImageJ software. Here, a median filter was created using the raw AFM image data. Subsequently, the median filter was subtracted from the original AFM image, resulting in an image with reduced background noise and more discernable NPs. Following the background subtraction, the image was binarized and subsequently analyzed using the "Analyze Particles" function built into ImageJ to calculate the number density of NPs. Figure S6 shows the step-by-step image analysis for a representative as-cast 25/75 wt % PMMA-NP/ SAN film.

AFM nanoindentation measurements were performed in an Asylum MFP-3D (Oxford Instruments/Asylum Research, Santa Barbara, CA) under ambient air temperature and humidity after completion of the annealing treatment if applicable. As such, the imaged morphologies are kinetically trapped, preventing further phase development. Tapping mode AFM probes coated in hard tetrahedral amorphous carbon (Tap300DLC, Budget Sensors, Sofia, Bulgaria) were used to minimize tip wear across many indentation cycles and allow for adequate resolution of sample deformation in the indentation tests. Images were acquired in the amplitude modulation (a.k.a. "tapping") mode, before and after indentations to ensure each region was representative of the sample and to confirm the location of each indent. Indentations were performed to a maximum load of 300-1200 nN, on grids of 10×10 locations spaced evenly across 2.0×2.0 μm^2 or 0.5 \times 0.5 μm^2 . A 2 s hold at the maximum applied load was implemented to allow time for rapid viscoelastic relaxation to complete. Indentation data was analyzed using the Oliver-Pharr technique.⁵⁸ The area function used in the analysis was determined

via TEM imaging of the tip apex with the assumption of axisymmetry around the tip's vertical axis. More information on the analysis method is included in the Supporting Information.

For comparisons of mechanical properties between films with different annealing treatments (Figure 2) or with different maximum indentation loads (Figure 3), the error bars are standard deviations that show the data spread, rather than standard error, which shows the likely range of the true mean value and would be an order of magnitude smaller. This was done because the films are inhomogeneous and that inhomogeneity depends on the annealing treatment, as discussed in detail in the manuscript. The overlap of the error bars does raise the question of whether the differences are statistically significant, however. To address this, statistical tests of these distributions were performed. A one-way analysis of variance (ANOVA) test of reduced modulus values in Figure 2b, 59 where the error bar overlap is more severe than in the hardness values, shows that F = 31.2, and $F_{crit} = 3.0$, so $F > F_{crit}$ and the three populations are not all equal. The p-value for this set of measurements is 1.3×10^{-13} , which is below any reasonable significance level. Given that this is true, we can do a post hoc t-test assuming equal variances, comparing each set of tests. The difference between the means in each comparison is significant, with the least significant pair, 150 °Cannealed vs 190 °C-annealed, having t(397) = -3.71, p < 0.00024. For Figure 3, we do make the claim that the property enhancement is more dramatic at shallower maximum indentation depths i.e., the difference between annealed and as-cast films is larger at 300 nN than at 1200 nN. While this is visually obvious, this is only true if the difference between the properties of the annealed sample at these two loads is statistically significant. Running the ANOVA tests again for the reduced modulus on the annealed sample where the error bar overlap is most severe and the trend is subtle, across all three indentation loads, F = 30.2, and $F_{crit} = 3.0$, so $F > F_{crit}$ and the three populations are not all equal. The p-value for this set of measurements is 1.2×10^{-12} , which is below any reasonable significance level. The post hoc T-test shows that the comparison between 300 or 600 and 1200 nN is statistically significant, with $p < 2 \times 10^{-11}$ in both cases. The trends in hardness with increasing indentation depth are more robust, with clear and statistically significant trends across all three loads for both the as-cast and annealed films.

ASSOCIATED CONTENT

Supporting Information

The Supporting Information is available free of charge at https://pubs.acs.org/doi/10.1021/acsami.2c15786.

> TEM analysis to determine PMMA-NP core diameter within ultramicrotomed slices, discussion of AFM nanoindentation fitting procedure, additional AFM nanoindentation results for control samples, AFM nanomilling procedure, AFM image analysis to extract NP number density, discussion on the improved thermal stability mechanism, and a discussion on different structure-property relations utilizing the presented self-regulated PNC film morphologies (PDF)

AUTHOR INFORMATION

Corresponding Authors

Robert W. Carpick - Department of Mechanical Engineering and Applied Mechanics, University of Pennsylvania, Philadelphia, Pennsylvania 19104, United States; orcid.org/0000-0002-3235-3156; Email: carpick@ seas.upenn.edu

Russell J. Composto - Department of Materials Science and Engineering, University of Pennsylvania, Philadelphia, Pennsylvania 19104, United States; o orcid.org/0000-0002-5906-2594; Email: composto@seas.upenn.edu

Authors

Shawn M. Maguire - Department of Materials Science and Engineering, University of Pennsylvania, Philadelphia, Pennsylvania 19104, United States; Present Address: Department of Chemical and Biological Engineering, Princeton University, Princeton, New Jersey 08544, United States; o orcid.org/0000-0002-5317-4990

J. Brandon McClimon - Department of Mechanical Engineering and Applied Mechanics, University of Pennsylvania, Philadelphia, Pennsylvania 19104, United

Aria C. Zhang - Department of Materials Science and Engineering, University of Pennsylvania, Philadelphia, Pennsylvania 19104, United States

Austin W. Keller - Department of Materials Science and Engineering, University of Pennsylvania, Philadelphia, Pennsylvania 19104, United States; Present Address: Micron Semiconductor, Inc., 8000 S Federal Way, Boise, Idaho 83707, United States.; oorcid.org/ 0000-0003-1288-7027

Connor R. Bilchak - Department of Materials Science and Engineering, University of Pennsylvania, Philadelphia, Pennsylvania 19104, United States; Present Address: Department of Chemical Engineering, Manhattan College, Bronx, New York 10471, United States.; o orcid.org/0000-0001-8815-1601

Kohji Ohno - Department of Materials Science, Graduate School of Engineering, Osaka Metropolitan University, Sakai, Osaka 599-8531, Japan; orcid.org/0000-0002-1812-3354

Complete contact information is available at: https://pubs.acs.org/10.1021/acsami.2c15786

Author Contributions

 $^{
abla}$ S.M.M. and J.B.M. contributed equally to this work. R.J.C. and R.W.C. designed and supervised this work. K.O. synthesized the nanoparticles used in this study. S.M.M., J.B.M., A.C.Z., A.W.K., and C.R.B. carried out experiments. S.M.M. and J.B.M. analyzed experimental results. S.M.M. and J.B.M. prepared schematics. The manuscript was written and edited through contributions of all authors. All authors have given approval to the final version of the manuscript.

Notes

The authors declare no competing financial interest.

ACKNOWLEDGMENTS

S.M.M., A.C.Z., C.R.B., and R.J.C. were supported by the National Science Foundation Partnerships for International Research and Education Program (NSF-PIRE), Grant #1545884. This work was also supported by the POLY-MERS-DMR-1905912 (S.M.M., C.R.B., R.J.C.) and MRSEC-DMR-1720530 (S.M.M., J.B.M., C.R.B., R.J.C., R.W.C.) programs. A.W.K. acknowledges funding from the Semiconductor Research Corporation (SRC), Task 2797.001. A.C.Z. acknowledges funding from an NSF Graduate Fellowship. K.O. acknowledges the funding from the Japan Society for the Promotion of Science (JSPS) KAKENHI Grants (no. 21H02000). This work was carried out in part at the Singh Center for Nanotechnology, which is supported by the NSF National Nanotechnology Coordinated Infrastructure Program under Grant NNCI-2025608. The authors gratefully acknowledge the use of facilities and instrumentation (TGA, DSC,

OM) supported by the Materials Science and Engineering Departmental Laboratory at the University of Pennsylvania. The authors thank Dr. Karen I. Winey for use of her laboratory's ultramicrotome, as well as Cherie R. Kagan and Christopher B. Murray for use of their TEM and expertise. Additionally, the authors acknowledge Sahana Sundar for performing DDSCAT simulations, as well as Dr. Kevin T. Turner and Sage Fulco for their expertise and collaboration in performing standard AFM nanoindentation. The authors also acknowledge Dr. Robert A. Riggleman, Dr. Daeyeon Lee, and Dr. Patrice Rannou for helpful discussions.

REFERENCES

- (1) Jancar, J.; Douglas, J. F.; Starr, F. W.; Kumar, S. K.; Cassagnau, P.; Lesser, A. J.; Sternstein, S. S.; Buehler, M. J. Current Issues in Research on Structure-Property Relationships in Polymer Nanocomposites. *Polymer* **2010**, *51*, 3321–3343.
- (2) Moll, J. F.; Akcora, P.; Rungta, A.; Gong, S.; Colby, R. H.; Benicewicz, B. C.; Kumar, S. K. Mechanical Reinforcement in Polymer Melts Filled with Polymer Grafted Nanoparticles. *Macromolecules* **2011**, *44*, 7473–7477.
- (3) Fu, S.; Sun, Z.; Huang, P.; Li, Y.; Hu, N. Some Basic Aspects of Polymer Nanocomposites: A Critical Review. *Nano Mater. Sci.* **2019**, 1, 2–30.
- (4) Díez-Pascual, A. M.; Gómez-Fatou, M. A.; Ania, F.; Flores, A. Nanoindentation in Polymer Nanocomposites. *Prog. Mater. Sci.* **2015**, 67, 1–94.
- (5) Quaresimin, M.; Bertani, R.; Zappalorto, M.; Pontefisso, A.; Simionato, F.; Bartolozzi, A. Multifunctional Polymer Nanocomposites with Enhanced Mechanical and Anti-Microbial Properties. *Composites, Part B* **2015**, *80*, 108–115.
- (6) Shah, T.; Gupta, C.; Ferebee, R. L.; Bockstaller, M. R.; Washburn, N. R. Extraordinary Toughening and Strengthening Effect in Polymer Nanocomposites Using Lignin-Based Fillers Synthesized by ATRP. *Polymer* 2015, 72, 406–412.
- (7) Midya, J.; Cang, Y.; Egorov, S. A.; Matyjaszewski, K.; Bockstaller, M. R.; Nikoubashman, A.; Fytas, G. Disentangling the Role of Chain Conformation on the Mechanics of Polymer Tethered Particle Materials. *Nano Lett.* **2019**, *19*, 2715–2722.
- (8) Cheng, S.; Bocharova, V.; Belianinov, A.; Xiong, S.; Kisliuk, A.; Somnath, S.; Holt, A. P.; Ovchinnikova, O. S.; Jesse, S.; Martin, H.; Etampawala, T.; Dadmun, M.; Sokolov, A. P. Unraveling the Mechanism of Nanoscale Mechanical Reinforcement in Glassy Polymer Nanocomposites. *Nano Lett.* **2016**, *16*, 3630–3637.
- (9) Lenart, W. R.; Hore, M. J. A. Structure—Property Relationships of Polymer-Grafted Nanospheres for Designing Advanced Nanocomposites. *Nano-Struct. Nano-Objects* **2018**, *16*, 428–440.
- (10) Sun, L.; Gibson, R. F.; Gordaninejad, F.; Suhr, J. Energy Absorption Capability of Nanocomposites: A Review. *Compos. Sci. Technol.* **2009**, *69*, 2392–2409.
- (11) Huang, Y.-R.; Jiang, Y.; Hor, J. L.; Gupta, R.; Zhang, L.; Stebe, K. J.; Feng, G.; Turner, K. T.; Lee, D. Polymer Nanocomposite Films with Extremely High Nanoparticle Loadings via Capillary Rise Infiltration (CaRI). *Nanoscale* **2015**, *7*, 798–805.
- (12) Sangermano, M.; Messori, M. Scratch Resistance Enhancement of Polymer Coatings. *Macromol. Mater. Eng.* **2010**, 295, 603–612.
- (13) Burris, D. L.; Boesl, B.; Bourne, G. R.; Sawyer, W. G. Polymeric Nanocomposites for Tribological Applications. *Macromol. Mater. Eng.* **2007**, 292, 387–402.
- (14) Roppolo, I.; Sangermano, M.; Chiolerio, A. Optical Properties of Polymer Nanocomposites. *Funct. Phys. Prop. Polym. Nanocompos.* **2016**, *31*, 139–157.
- (15) Hore, M. J. A. Predicting the Optical and Electrical Properties of Polymer Nanocomposites. In *Theory and Modeling of Polymer Nanocomposites*; Ginzburg, V. V.; Hall, L. M., Eds.; Springer, 2021.
- (16) Dang, A.; Ojha, S.; Hui, C. M.; Mahoney, C.; Matyjaszewski, K.; Bockstaller, M. R. High-Transparency Polymer Nanocomposites

- Enabled by Polymer- Graft Modification of Particle Fillers. *Langmuir* **2014**, *30*, 14434–14442.
- (17) Wang, Z.; Lu, Z.; Mahoney, C.; Yan, J.; Ferebee, R.; Luo, D.; Matyjaszewski, K.; Bockstaller, M. R. Transparent and High Refractive Index Thermoplastic Polymer Glasses Using Evaporative Ligand Exchange of Hybrid Particle Fillers. ACS Appl. Mater. Interfaces 2017, 9, 7515–7522.
- (18) Merkel, T. C.; Freeman, B. D.; Spontak, R. J.; He, Z.; Pinnau, I.; Meakin, P.; Hill, aJ. Ultrapermeable, Reverse-Selective Nanocomposite Membranes. *Science* **2002**, *296*, 519–522.
- (19) Bilchak, C. R.; Jhalaria, M.; Huang, Y.; Abbas, Z.; Midya, J.; Benedetti, F. M.; Parisi, D.; Egger, W.; Dickmann, M.; Minelli, M.; Doghieri, F.; Nikoubashman, A.; Durning, C. J.; Vlassopoulos, D.; Jestin, J.; Smith, Z. P.; Benicewicz, B. C.; Rubinstein, M.; Leibler, L.; Kumar, S. K. Tuning Selectivities in Gas Separation Membranes Based on Polymer-Grafted Nanoparticles. *ACS Nano* **2020**, *14*, 17174–17183.
- (20) Bilchak, C. R.; Buenning, E.; Asai, M.; Zhang, K.; Durning, C. J.; Kumar, S. K.; Huang, Y.; Benicewicz, B. C.; Gidley, D. W.; Cheng, S.; Sokolov, A. P.; Minelli, M.; Doghieri, F. Polymer-Grafted Nanoparticle Membranes with Controllable Free Volume. *Macromolecules* **2017**, *50*, 7111–7120.
- (21) Jeong, S. P.; Kumar, R.; Genix, A. C.; Popov, I.; Li, C.; Mahurin, S. M.; Hu, X.; Bras, W.; Popovs, I.; Sokolov, A. P.; Bocharova, V. Improving Gas Selectivity in Membranes Using Polymer-Grafted Silica Nanoparticles. *ACS Appl. Nano Mater.* **2021**, *4*, 5895–5903.
- (22) Bocharova, V.; Sokolov, A. P. Perspectives for Polymer Electrolytes: A View from Fundamentals of Ionic Conductivity. *Macromolecules* **2020**, *53*, 4141–4157.
- (23) Choudhury, S.; Mangal, R.; Agrawal, A.; Archer, L. A. A Highly Reversible Room-Temperature Lithium Metal Battery Based on Crosslinked Hairy Nanoparticles. *Nat. Commun.* **2015**, *6*, No. 10101.
- (24) Glynos, E.; Papoutsakis, L.; Pan, W.; Giannelis, E. P.; Nega, A. D.; Mygiakis, E.; Sakellariou, G.; Anastasiadis, S. H. Nanostructured Polymer Particles as Additives for High Conductivity, High Modulus Solid Polymer Electrolytes. *Macromolecules* **2017**, *50*, 4699–4706.
- (25) Maréchal, M.; Niepceron, F.; Gebel, G.; Mendil-Jakani, H.; Galiano, H. Inside the Structure of a Nanocomposite Electrolyte Membrane: How Hybrid Particles Get along with the Polymer Matrix. *Nanoscale* **2015**, *7*, 3077–3087.
- (26) Sasaki, N.; Umeda, H.; Okada, S.; Kojima, R.; Fukuda, A. Mechanical Properties of Hydroxyapatite-Reinforced Gelatin as a Model System of Bone. *Biomaterials* 1989, 10, 129–132.
- (27) Sasaki, N.; Yamamura, H.; Matsushima, N. Is There a Relation between Bone Strength and Percolation? *J. Theor. Biol.* **1986**, 122, 25–31.
- (28) Barthelat, F. Biomimetics for next Generation Materials. *Philos. Trans. R. Soc. A* **2007**, 365, 2907–2919.
- (29) Shanmuganathan, K.; Capadona, J. R.; Rowan, S. J.; Weder, C. Biomimetic Mechanically Adaptive Nanocomposites. *Prog. Polym. Sci.* **2010**, 35, 212–222.
- (30) Cudjoe, E.; Khani, S.; Way, A. E.; Hore, M. J. A.; Maia, J.; Rowan, S. J. Biomimetic Reversible Heat-Stiffening Polymer Nanocomposites. *ACS Cent. Sci.* **2017**, *3*, 886–894.
- (31) Lee, H.; Dellatore, S. M.; Miller, W. M.; Messersmith, P. B. Mussel-Inspired Surface Chemistry for Multifunctional Coatings. *Science* **2007**, *318*, 426–430.
- (32) Jeong, K. J.; Wang, L.; Stefanescu, C. F.; Lawlor, M. W.; Polat, J.; Dohlman, C. H.; Langer, R. S.; Kohane, D. S. Polydopamine Coatings Enhance Biointegration of a Model Polymeric Implant. *Soft Matter* **2011**, *7*, 8305–8312.
- (33) Kung, M. L.; Lin, P. Y.; Peng, S. W.; Wu, D. C.; Wu, W. J.; Yeh, B. W.; Tai, M. H.; Hung, H. S.; Hsieh, S. Biomimetic Polymer-Based Ag Nanocomposites as a Antimicrobial Platform. *Appl. Mater. Today* **2016**, *4*, 31–39.
- (34) Sung, K.; Nakagawa, S.; Yoshie, N. Fabrication of Water-Resistant Nacre-like Polymer/Clay Nanocomposites via in Situ Polymerization. *ACS Omega* **2017**, *2*, 8475–8482.

- (35) Podsiadlo, P.; Liu, Z.; Paterson, D.; Messersmith, P. B.; Kotov, N. A. Fusion of Seashell Nacre and Marine Bioadhesive Analogs: High-Strength Nanocomposite by Layer-by-Layer Assembly of Clay and L-3,4- Dihydroxyphenylalanine Polymer. Adv. Mater. 2007, 19,
- (36) Podsiadlo, P.; Kaushik, A. K.; Shim, B. S.; Agarwal, A.; Tang, Z.; Waas, A. M.; Arruda, E. M.; Kotov, N. A. Can Nature's Design Be Improved upon? High Strength, Transparent Nacre-like Nanocomposites with Double Network of Sacrificial Cross Links. J. Phys. Chem. B 2008, 112, 14359-14363.
- (37) Zhao, D.; Gimenez-Pinto, V.; Jimenez, A. M.; Zhao, L.; Jestin, J.; Kumar, S. K.; Kuei, B.; Gomez, E. D.; Prasad, A. S.; Schadler, L. S.; Khani, M. M.; Benicewicz, B. C. Tunable Multiscale Nanoparticle Ordering by Polymer Crystallization. ACS Cent. Sci. 2017, 3, 751-
- (38) Maguire, S. M.; Boyle, M. J.; Bilchak, C. R.; Demaree, J. D.; Keller, A. W.; Krook, N. M.; Ohno, K.; Kagan, C. R.; Murray, C. B.; Rannou, P.; Composto, R. J. Grafted Nanoparticle Surface Wetting during Phase Separation in Polymer Nanocomposite Films. ACS Appl. Mater. Interfaces 2021, 13, 37628-37637.
- (39) Maguire, S. M.; Krook, N. M.; Kulshreshtha, A.; Bilchak, C. R.; Brosnan, R.; Pana, A. M.; Rannou, P.; Maréchal, M.; Ohno, K.; Jayaraman, A.; Composto, R. J. Interfacial Compatibilization in Ternary Polymer Nanocomposites: Comparing Theory and Experiments. Macromolecules 2021, 54, 797-811.
- (40) Maguire, S. M.; Demaree, J. D.; Boyle, M. J.; Keller, A. W.; Bilchak, C. R.; Kagan, C. R.; Murray, C. B.; Ohno, K.; Composto, R. J. Surface-Enrichment of Polymer Grafted Nanoparticles in a Miscible Polymer Nanocomposite. Macromolecules 2022, 55, 7724-7731.
- (41) Chung, H. J.; Wang, H.; Composto, R. J. A Morphology Map Based on Phase Evolution in Polymer Blend Films. Macromolecules 2006, 39, 153-161.
- (42) Oliver, W. C.; Pharr, G. M. Measurement of Hardness and Elastic Modulus by Instrumented Indentation: Advances in Understanding and Refinements to Methodology. J. Mater. Res. 2004, 19,
- (43) Johnson, K. L. The Correlation of Indentation Experiments. J. Mech. Phys. Solids 1970, 18, 115-126.
- (44) Tweedie, C. A.; Van Vliet, K. J. On the Indentation Recovery and Fleeting Hardness of Polymers. J. Mater. Res. 2006, 21, 3029-3036.
- (45) Schmitt, M.; Zhang, J.; Lee, J.; Lee, B.; Ning, X.; Zhang, R.; Karim, A.; Davis, R. F.; Matyjaszewski, K.; Bockstaller, M. R. Polymer Ligand-Induced Autonomous Sorting and Reversible Phase Separation in Binary Particle Blends. Sci. Adv. 2016, 2, No. e1601484.
- (46) Lucas, M.; Gall, K.; Riedo, E. Tip Size Effects on Atomic Force Microscopy Nanoindentation of a Gold Single Crystal. J. Appl. Phys. 2008, 104, No. 113515.
- (47) Maguire, S. M.; Bilchak, C. R.; Corsi, J. S.; Welborn, S. S.; Tsaggaris, T.; Ford, J.; Detsi, E.; Fakhraai, Z.; Composto, R. J. Effect of Nanoscale Confinement on Polymer-Infiltrated Scaffold Metal Composites. ACS Appl. Mater. Interfaces 2021, 13, 44893-44903.
- (48) Krishnan, R. S.; Mackay, M. E.; Duxbury, P. M.; Hawker, C. J.; Asokan, S.; Wong, M. S.; Goyette, R.; Thiyagarajan, P. Improved Polymer Thin-Film Wetting Behavior through Nanoparticle Segregation to Interfaces. J. Phys.: Condens. Matter 2007, 19, No. 356003.
- (49) McGarrity, E. S.; Frischknecht, A. L.; Frink, L. J. D.; MacKay, M. E. Surface-Induced First-Order Transition in Athermal Polymer-Nanoparticle Blends. Phys. Rev. Lett. 2007, 99, No. 238302.
- (50) Briggs, D.; Hearn, M. J.; Chan, H.; McBriar, D. I.; Munro, H. S. The Contact Angle of Poly(Methyl Methacrylate) Cast against Glass. Langmuir 1990, 6, 420-424.
- (51) Horinouchi, A.; Atarashi, H.; Fujii, Y.; Tanaka, K. Dynamics of Water-Induced Surface Reorganization in Poly(Methyl Methacrylate) Films. Macromolecules 2012, 45, 4638-4642.
- (52) Fernández-Rico, C.; Sai, T.; Sicher, A.; Style, R. W.; Dufresne, E. R. Putting the Squeeze on Phase Separation. JACS Au 2022, 2, 66-73.

- (53) Medina, J. M.; Díaz, J. A.; Vukusic, P. Classification of Peacock Feather Reflectance Using Principal Component Analysis Similarity Factors from Multispectral Imaging Data. Opt. Express 2015, 23, No. 010198.
- (54) Lange, H.; Juárez, B. H.; Carl, A.; Richter, M.; Bastús, N. G.; Weller, H.; Thomsen, C.; Von Klitzing, R.; Knorr, A. Tunable Plasmon Coupling in Distance-Controlled Gold Nanoparticles. Langmuir 2012, 28, 8862-8866.
- (55) Yoon, J. H.; Selbach, F.; Schumacher, L.; Jose, J.; Schlücker, S. Surface Plasmon Coupling in Dimers of Gold Nanoparticles: Experiment and Theory for Ideal (Spherical) and Nonideal (Faceted) Building Blocks. ACS Photonics 2019, 6, 642-648.
- (56) Gam, S.; Corlu, A.; Chung, H.-J.; Ohno, K.; Hore, M. J. A.; Composto, R. J. A Jamming Morphology Map of Polymer Blend Nanocomposite Films. Soft Matter 2011, 7, 7262.
- (57) Ohno, K.; Morinaga, T.; Koh, K.; Tsujii, Y.; Fukuda, T. Synthesis of Monodisperse Silica Particles Coated with Well-Defined, High-Density Polymer Brushes by Surface-Initiated Atom Transfer Radical Polymerization. Macromolecules 2005, 38, 2137-2142.
- (58) Oliver, W. C.; Pharr, G. M. An Improved Technique for Determining Hardness and Elastic Modulus Using Load and Displacement Sensing Indentation Experiments. J. Mater. Res. 1992, 7, 1564-1583.
- (59) Brady, S. M.; Burow, M.; Busch, W.; Carlborg, O.; Denby, K. J.; Glazebrook, J.; Hamilton, E. S.; Harmer, S. L.; Haswell, E. S.; Maloof, J. N.; Springer, N. M.; Kliebenstein, D. J. Reassess the t Test: Interact with All Your Data via ANOVA. Plant Cell 2015, 27, 2088-2094.

□ Recommended by ACS

Understanding the Rheology of Polymer-Polymer Interfaces Covered with Janus Nanoparticles: Polymer Blends versus **Particle Sandwiched Multilayers**

Huawei Qiao, Huagui Zhang, et al.

JANUARY 02, 2023

MACROMOLECULES

RFAD 🗹

Revealing the Shear Effect on the Interfacial Layer in Polymer Nanocomposites through Nanofiber Reorientation

Benke Li, Wei Yu, et al.

APRIL 12, 2023

MACROMOLECULES

READ

Chain Movements at the Topmost Surface of Poly(methyl methacrylate) and Polystyrene Films Directly Evaluated by In Situ High-Temperature Atomic Force Microscopy

Kouki Koike and Jiro Kumaki

NOVEMBER 01, 2022

LANGMUIR

READ **C**

Crystallization Kinetics and Mechanical Properties of Miscible Polymer Blend Nanocomposites: Linear versus **Grafted Systems**

Abdullah S. Altorbaq, Sanat K. Kumar, et al.

SEPTEMBER 02, 2022

MACROMOLECULES

RFAD 🗹

Get More Suggestions >